Dalton Transactions

ROYAL SOCIETY OF CHEMISTRY

PAPER

View Article Online
View Journal | View Issue

Open Access Article. Published on 16 October 2025. Downloaded on 12/28/2025 10:30:21 AM.
This article is licensed under a Creative Commons Attribution-NonCommercial 3.0 Unported Licence.

Check for updates

Cite this: *Dalton Trans.*, 2025, **54**, 16177

Exploring early transition metal coordination: a synthetic and computational study of tripodal ligand complexes

Jewelianna M. Moore,[a] Brennan M. Vaught,[a] Tabitha J. Miller,[b] George Nunn,[c] Lindsey S. Elford,[a] Kelly L. Gullett,[b] Paul H. Walton[c] and Alison R. Fout*[a]

Received 7th August 2025,
Accepted 29th September 2025

DOI: 10.1039/d5dt01888a

rsc.li/dalton

A series of early transition metal complexes supported by the tripodal ligand tris(5-cyclohexyl-imminopyrrol-2-ylmethyl)amine ($N(pi^{Cy})_3$) were synthesized and characterized to investigate their structural and electronic properties. Complexes of titanium, vanadium, chromium, and molybdenum reveal diverse coordination geometries and highlight the influence of metal identity on geometry. Spectroscopic and computational analyses demonstrate predictable periodic trends in metal–ligand bond lengths. These results underscore the structural versatility of the $N(pi^{Cy})_3$ ligand and its utility in supporting a range of early transition metal centers.

Introduction

Nature employs a diverse array of metal ions, particularly abundant first-row transition metals and molybdenum, for essential biological functions such as protein scaffolding, electron transfer, substrate binding, and catalysis.[1,2] The importance of metal ions is well known in biology; it is estimated that 47% of human enzymes require a metal site to properly function.[3] Among transition metals, iron is the most widely incorporated redox-active metal, essential for processes such as oxidoreduction reactions and oxygen transport in hemoglobin.[4–6]

While Nature heavily utilizes redox active iron, certain early transition metals exhibit reactivity rarely observed in later transition metals. Molybdenum is essential for nearly all organisms,[7] with few exceptions that instead rely on its third-row equivalent, tungsten.[8] One of the most well-known molybdenum-dependent enzymes is molybdenum nitrogenase, essential to biological nitrogen fixation.[9] Notably, an iron-based nitrogenase also exists, exhibiting only one-third the reactivity of its molybdenum counterpart.[10]

Beyond molybdenum's role in the nitrogen geochemical cycle, it is also essential in the carbon and sulfur geochemical cycles.[11] Molybdopterin enzymes are classified into three groups based on the ligand environment around the Mo centre: xanthine oxidase, sulfite oxidase, and dimethyl sulfoxide (DMSO) reductase families.[12] Each family catalyses similar two electron redox reactions, facilitating processes such as the reduction of nitrate to nitrite and the oxidation of sulfite to sulfate, both transformations that native iron-based enzymes cannot achieve.[13,14] In addition to molybdenum, other early transition metals, namely vanadium[15,16] and chromium,[17] are essential for a variety of processes across different organisms, including vanadium's role in vanadium nitrogenase.

Despite Nature's inclusion of a diverse set of metals, much of the synthetic work conducted by bioinorganic chemists has focused on mid to late transition metals, particularly on iron, due to its ubiquity in nature.[18–22] For instance, previous work carried out by our group centred on the synthesis and reactivity of mid to late transition metal complexes featuring the tripodal ligand tris(5-cyclohexylimminopyrrol-2-ylmethyl)amine ($N(pi^{Cy})_3$). $N(pi^{Cy})_3$ is easily metalated upon addition of Fe$(OTf)_2(MeCN)_2$, forming the ligand tautomerized complex, $[(N(afa^{Cy})_3)Fe]OTf_2$ (OTf = triflate).[23,24] $[(N(afa^{Cy})_3)Fe]OTf_2$ successfully reproduces the reactivity of several oxyanion reduction enzymes, including those in the molybdenum dependent DMSO reductase family. This complex is part of a wider family of catalysts published by our group which exhibit the reduction of nitrate and nitrite selectively to nitric oxide, ammonia, or nitrogen, perchlorate to chloride, and selenate to red elemental selenium.[24–29]

In contrast to the previously discussed metalation strategy of the neutral $N(pi^{Cy})_3$ ligand, which gives Fe(II) complexes with trigonal bipyramidal geometries, we developed an alternative metalation approach for synthesizing an Fe(III) complex, $(N(pi^{Cy})_3)Fe$ (**1-Fe**) through deprotonation of $N(pi^{Cy})_3$ with 3.1 equivalents of potassium hydride (KH) to generate the ligand

[a]*Department of Chemistry, Texas A&M University, College Station, Texas 77843, USA. E-mail: fout@tamu.edu*
[b]*School of Chemical Sciences, University of Illinois at Urbana–Champaign, Urbana, Illinois 61801, USA*
[c]*Department of Chemistry, University of York, Heslington, York, YO10 5DD, UK*

Open Access Article. Published on 16 October 2025. Downloaded on 12/28/2025 10:30:21 AM. This article is licensed under a Creative Commons Attribution-NonCommercial 3.0 Unported Licence.

salt, $K_3[N(pi^{Cy})_3]$, followed by addition of iron(III) chloride to generate **1-Fe**.[23] Structural analysis revealed a distinct pseudo-octahedral geometry at the iron centre, coordinated by $N_{pyrrole}$ and N_{imine} nitrogen atoms. This contrasts with previously reported Fe(II) complexes of $N(pi^{Cy})_3$, which utilize the N_{apical} atom for metal binding.[23]

Building on our previous iron focused work with $N(pi^{Cy})_3$, we aimed to install several early transition metals in the tripodal ligand framework, which may offer different reactivity compared to the well investigated iron complexes. Molybdenum and vanadium, both biologically relevant and abundant transition metals, were of particular interest. Herein, we present a series of analogous metal complexes featuring trivalent early transition metals. Trivalent complexes were targeted for several reasons: (1) the octahedral ligand environment $N(pi^{Cy})_3$ can adopt provides a synthetically facile route to early transition metal complexes with our system; (2) these complexes may exhibit reactivity not achieved with any of our previously reported iron complexes; and (3) they enable direct structural and electronic comparisons to the previously reported **1-Fe**.[23] Through synthesising a range of early transition metal complexes within a well-established ligand framework, we create the opportunity to compare various biologically relevant metals. This approach also highlights the adaptability of the tripodal ligand system $N(pi^{Cy})_3$.

Results and discussion

The syntheses of these early metal complexes were carried out by targeting the trivalent octahedral complexes, analogous to the reported $(N(pi^{Cy})_3)Fe$ (**1-Fe**) complex.[23] For titanium ($(N(pi^{Cy})_3)Ti$ (**1-Ti**)), vanadium ($(N(pi^{Cy})_3)V$ (**1-V**)), and molybdenum ($(N(pi^{Cy})_3)Mo$ (**1-Mo**)), metalation was achieved through an adapted literature procedure of **1-Fe** (Scheme 1). To a solution of the triply deprotonated ligand was added $MCl_3(THF)_3$ (M = **Ti**, **V**, **Mo** and THF = tetrahydrofuran). Stirring for 2 hours resulted in dark-green solutions for titanium and vanadium and a red-brown solution for molybdenum. Each complex was washed well with hexanes and isolated by extraction with ether in moderate to good yields (57.9–81.5%).

While the analogous chromium complex, $(N(pi^{Cy})_3)Cr$ (**1-Cr**), can be synthesized using $CrCl_3$, poor solubility necessitated long reaction times (>20 hours) and poor yields. The chromium complex **1-Cr** was instead synthesized by treatment of $Cr(N(TMS)_2)_3$ (TMS = trimethylsilyl) with a solution of the neutral ligand, resulting in a slow colour change from deep green to a vibrant red over the course of 4 hours (Scheme 1). A bright red/pink powder was isolated by extraction with hexanes in good yield (91.4%).

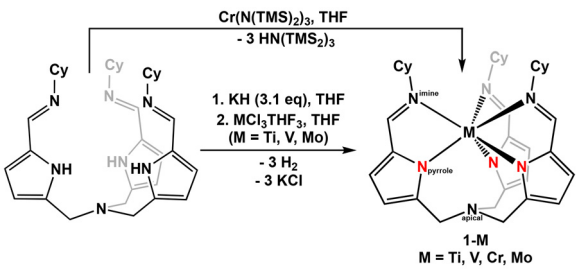

Scheme 1 Metalation strategies to synthesize **1-Ti, V, Cr, Mo**.

Each complex was characterized using a range of spectroscopic methods. Infrared spectroscopy gave insight to the binding of the metal ion to the ligand framework. Complexes **1-Ti, V, Cr, Mo** exhibited C=N stretches of 1577, 1577, 1566, 1570 cm^{-1}, respectively, in the infrared spectra. **1-Fe** exhibited a similar C=N stretch of 1581 cm^{-1},[23] which we have identified as a characteristic C=N stretch when the metal ion binds to the ligand hexadentate, remaining unbound to the apical nitrogen.[23,30,31] In contrast, when the ligand is bound tetradentate, the ligand C=N stretch sits above 1600 cm^{-1}.[23,24]

Although these complexes are all paramagnetic, their ^1H NMR spectra show marked differences. The ^1H NMR spectra of complexes **1-Ti** and **1-V** exhibit sharp resonances with minimal line broadening (Fig. S1 and S2, respectively). In contrast, the ^1H NMR spectrum of **1-Mo** (Fig. S4) exhibits significant line broadening, and the spectrum of **1-Cr** (Fig. S3) shows no detectable ^1H signals, likely due to severe line broadening. These differences arise from variations in electronic properties at the metal centre.

Complexes **1-Ti** and **1-V**, while paramagnetic, have lower magnetic moments of $1.85(11)\mu_B$ and $2.88(12)\mu_B$, respectively, compared to **1-Cr**, which has a higher magnetic moment of $3.71(11)\mu_B$ as determined by Evans' Method. The higher magnetic moment for **1-Cr** reflects a greater number of unpaired electrons, which increases the strength of the local magnetic field of the chromium centre, leading to faster T_1 and T_2 relaxation and more pronounced line broadening in the ^1H NMR spectrum.[32,33] The lower magnetic moment of **1-Ti** and **1-V**, conversely, results in weaker paramagnetic relaxation effects, resulting in sharper ^1H NMR resonances. However, the degree of line broadening is not governed solely by the number of unpaired electrons in a system. **1-Mo** experiences pronounced line broadening due to the stronger spin–orbit coupling of a second-row metal compared to a first-row metal.[34,35] As a result, electron relaxation is more efficient, the T_2 relaxation of nearby nuclei is faster, and signals are broadened in ^1H NMR spectra.

Given the strongly coloured powders isolated for each of these compounds, we anticipated observable d–d transitions in the electron absorption spectra. However, no absorbances that could be assigned to d–d transitions in spectra were visible, likely due to overlap with more intense ligand-based transitions. Given the high extinction coefficients for all observed absorbances, we assign these to be ligand-based absorbances, mainly π–π* transitions.

Single crystal X-ray diffraction of each complex confirmed coordination of the metal ion in a geometry distorted between octahedral and trigonal prismatic (Fig. 1). Refinement of the crystallographic data revealed the metal centres sat in a

 This journal is © The Royal Society of Chemistry 2025

Open Access Article. Published on 16 October 2025. Downloaded on 12/28/2025 10:30:21 AM. This article is licensed under a Creative Commons Attribution-NonCommercial 3.0 Unported Licence.

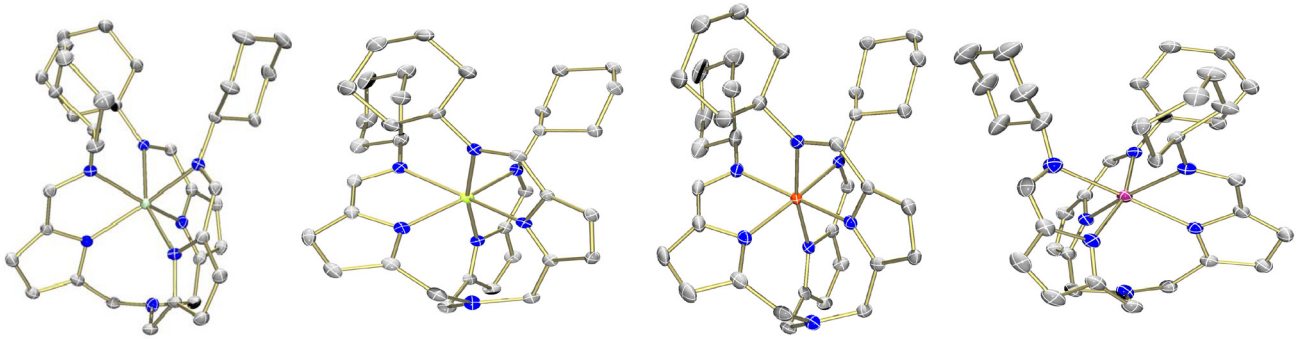

Fig. 1 Single crystal structures of **1-M** (M= Ti, V, Cr, Mo from left to right) at the 50% probability level. Outer sphere ether molecule in **1-Ti** and hydrogen atoms removed for clarity.

pseudo-octahedral facial ligand environment analogous to that of the reported structure of **1-Fe**.[23] Complexes **1-V**, **1-Cr**, and **1-Mo** are isostructural to one another, whereas **1-Ti** is not isostructural due to co-crystallization with a molecule of diethyl ether. A structural comparison of the complexes gave insight into how the metal centre effects binding to the ligand framework. The metal–nitrogen bond lengths exhibited the expected periodic trends, decreasing in length as the effective nuclear (Z_{eff}) charge increases across the first row of the periodic table (Table 1). Specifically, the M–N bond lengths decreased from **1-Ti** to **1-Cr** for the first-row complexes.

The previously published **1-Fe** complex displayed pronounced three-fold symmetry, setting it apart from the analogous early transition metal complexes. Compared to the early metal analogues, **1-Fe** exhibited consistently shorter M–N_{imine} bond lengths and longer M–$N_{pyrrole}$ bond lengths. Accordingly, the iron centre in **1-Fe** was positioned closer to the apical nitrogen, resulting in a more "in pocket" coordination geometry. This structural difference may arise from the smaller ionic radius of iron relative to early transition metals, allowing the Fe centre to fit more snugly within the ligand framework.

To gain more insight into the ligand field splitting of complexes **1-M**, computational calculations were performed. Complete-Active Space Self-Consistent Field (CASSCF) calculations were performed across all 5 3d (**1-Ti**, **1-V**, **1-Cr**, and **1-Fe**) or 4d (**1-Mo**) orbitals with N-Electron Valence Perturbation Theory (NEVPT2) corrections using ORCA version 5.0.2.[36–38] All complexes, besides **1-Mo**, were treated to be high-spin in their electronic configuration based on their experimental magnetic moments. The axes were oriented by placing the *z*-axis through the centre point of the three imine nitrogen atoms (see SI for in-depth computational details). For first-row complexes, the three lowest-lying d-orbitals were the d_{z_2}, d_{xy}, and $d_{x_2-y_2}$ with a considerable gap of ~2 eV to the higher d_{xz} and d_{yz} orbitals (Fig. 2). In the case of **1-Mo**, the energy gap was nearly 5 eV, correlating to stronger binding of molybdenum to nitrogen compared to its 3d congener **1-Cr**. This trend is well documented, as 4d and 5d metals have improved d-orbital overlap with ligands when compared to their 3d counterparts.[39] This stronger overlap can be observed in the generation of a low-spin species for **1-Mo**, different from **1-Cr**, even though both are d^3 complexes. Notably, for the earliest metal in the 3d series **1-Ti**, the lowest energy d-orbital was the $d_{x_2-y_2}$ orbital whereas all other complexes featured d_{z_2} as the lowest energy orbital.

For metal complexes with a coordination number of 6, two ideal geometries are possible: octahedral and trigonal prismatic. Using the computer program OctaDist 3.1.0,[40] deviations from a perfect octahedral coordination environment were calculated. Three parameters, ζ, Σ, and Θ are calculated and defined as follows: ζ – deviation of metal–ligand bond lengths from the average metal–ligand bond length of the complex; Σ – discrepancy of all *cis* ligand–metal–ligand bond angles from 90°; and, Θ – degree of torsional distortion from a perfect octahedron towards a trigonal prism.[40] For all parameters, values of 0 correlate to an ideal octahedral coordination geometry. Unsurprisingly, the complexes were heavily distorted from an ideal octahedron. In terms of ζ, the ordering from most to least octahedral was as follows: **1-V**, **1-Mo**, **1-Cr**, **1-Ti**, and **1-Fe**. For Σ and Θ, the order of the complexes is the same: **1-Mo**, **1-Cr**, **1-V**, **1-Fe**, and **1-Ti**. A complete table of distortion parameters can be found in the (Table S4).

Taking into consideration ζ, Σ, and Θ parameters, **1-Mo** had geometry closest to an ideal octahedron, followed by **1-Cr**, **1-V**, **1-Fe**, and, finally, **1-Ti**. The larger torsional distortion of **1-Ti** appears to allow $N_{pyrrole}$ and N_{imine} atoms better overlap with the d_{z_2} orbital. This may result in the higher energy for the anti-bonding d_{z_2} orbital of **1-Ti** compared to that for the other complexes.

Another trend was observed across the series of first-row metals: the energy gap between the 3 lower energy orbitals (d_{z_2}, $d_{x_2-y_2}$, and d_{xy}) and the two higher energy orbitals

Table 1 The average metal–nitrogen bond lengths in **1-M** (M = Ti, V, Cr, Mo, Fe)

	1-Ti	1-V	1-Cr	1-Mo	1-Fe
M–$N_{pyrrole}$ (Å)	2.24	2.17	2.12	2.21	2.26
M–N_{imine} (Å)	2.11	2.05	2.02	2.13	2.03
M–N_{apical} (Å)	3.20	3.51	3.55	3.33	2.95

Open Access Article. Published on 16 October 2025. Downloaded on 12/28/2025 10:30:21 AM.
This article is licensed under a Creative Commons Attribution-NonCommercial 3.0 Unported Licence.

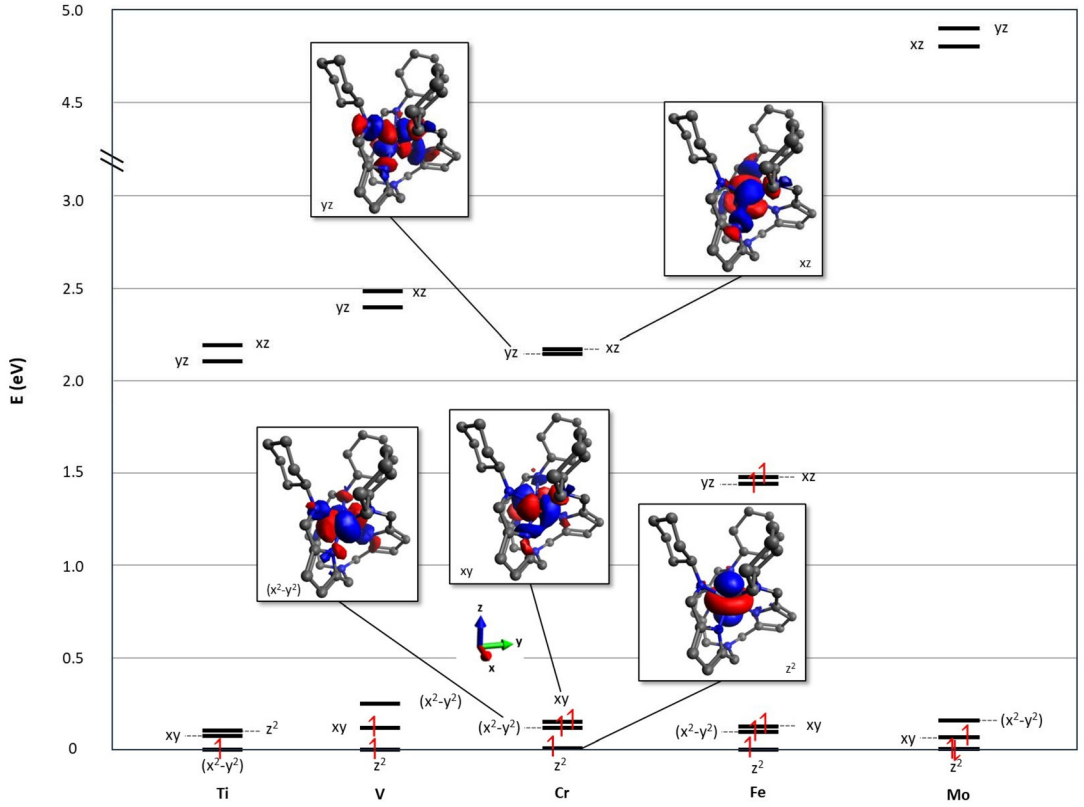

Fig. 2 Combined molecular orbital diagram generated from the ligand field one electron eigenfunctions given by the corresponding CASSCF calculations for **1-M**. For M = Ti, V, Cr, and Fe, orbitals are from the 3d shell and for M = Mo, the 4d shell. The orbitals of **1-Cr** are shown as insets to the orbital diagram. Individual graphical representations of the orbitals for each species are shown in Fig. S9–13.

(d_{xz} and d_{yz}) is smaller for **1-Fe**. When the higher energy orbitals are populated in **1-Fe**, metal–ligand σ-bonding orbitals are weakened, a trend observed by Gerloch and Deeth when analysing a series of trigonal–bipyramidal first-row complexes.[41] In total, the computations allowed a more in-depth look at how frontier electronic structure can be impacted both by d-electron count and deviation from a perfect coordination geometry.

Experimental

General considerations

Unless otherwise stated, all manipulations were carried out in an MBraun or Vigor inert atmosphere drybox under an atmosphere of nitrogen or using standard Schlenk techniques. All glassware was oven dried for a minimum of four hours and cooled in an evacuated antechamber prior to use. Solvents for air and moisture sensitive manipulations were dried and deoxygenated using a Glass Contour System (SG Water USA, Nashua, NH) and stored over 4 Å molecular sieves purchased from Strem prior to use. Celite 545 (J. T. Baker) was heated to 150 °C under dynamic vacuum for 24 h prior to use in the drybox. All reagents were purchased from commercial sources and used as received unless otherwise noted. Potassium hydride was purchased from Strem, washed with hexanes to remove mineral oil, and dried under vacuum prior to use. $H_3N(pi^{Cy})_3$[23] and $Cr(N(TMS)_2)_3$[42] were synthesized according to literature procedures. NMR solvents were purchased from Cambridge Isotope Laboratories, degassed, and stored over 4 Å molecular sieves prior to use.

NMR spectra were recorded at ambient temperature on a Varian spectrometer operating at 500 MHz (^{1}H NMR). All ^{1}H chemical shifts (ppm) are reported relative to the resonance of the residual solvent as a standard. Solid-state infrared spectra were measured using a PerkinElmer Frontier FT-IR spectrophotometer equipped with a KRS5 thallium bromide/iodide universal attenuated total reflectance accessory. Electronic absorption spectra were recorded on a Varian Cary 50 Bio spectrophotometer.

Quantum chemical considerations

Calculations on molecules were carried out using ORCA version 5.0.2.[36] Cartesian coordinates were imported from each molecules' respective X-ray crystal structure. For all calculations, the def2-TZVP basis set was applied to all atoms.[43] Geometry optimizations were performed with the BP86 functional along with the van der Waal correction D3BJ. Additionally, the solvation model CPCM was used to model the solvation effects of THF.[44] The /C auxiliary basis set and

 This journal is © The Royal Society of Chemistry 2025

Open Access Article. Published on 16 October 2025. Downloaded on 12/28/2025 10:30:21 AM. This article is licensed under a Creative Commons Attribution-NonCommercial 3.0 Unported Licence.

the RIJCOSX (chain of spheres) approximation was used to help improve the speed of the calculations.[45]

Ab initio calculations used Complete-Active Space Self-Consistent Field (CASSCF) and N-Electron Valence Perturbation Theory (NEVPT2).[37,38] These calculations were performed over the full number of configurational multiplicities and roots (see Table S1). Apart from complex **1-Mo**, the high-spin confirmation was selected as the ground state for all calculations. *Ab initio* Ligand Field Analysis (AILFT) was carried out after the NEVPT2 correction of the CASSCF calculation. The resulting orbitals were visualized using Avogadro 1.2.0.[46]

General preparation of 1-M (M = Ti, V, Mo)

A 20 mL scintillation vial equipped with a stir bar was charged with $N(pi^{Cy})_3$ (29.2 mg, 0.05 mmol) and KH (6.2 mg, 0.155 mmol, 3.1 equiv.) in tetrahydrofuran (4 mL). After stirring for 16 hours, the reaction was filtered through Celite to remove unreacted KH. To the filtrate was added $MCl_3(THF)_3$ (0.05 mmol). After stirring for 2 hours, volatiles were removed under reduced pressure. The resulting powder was washed with hexanes (3 × 1.5 mL), the product was dissolved in ether and filtered through Celite. Volatiles were removed under reduced pressure to yield a powder in moderate to good yield.

Synthesis of $(N(pi^{Cy})_3)$Ti (1-Ti)

The product was isolated as a green powder in moderate yield (64%). Crystals suitable for X-ray diffraction were grown from a concentrated ether solution of the green powder at −35 °C. HRMS (ESI) calcd for $[M]^+$: 626.3445 found: 626.3430. IR: 1577 cm^{-1} (C═N). μ_{eff} = 1.85(11)μ_B. UV-vis (THF, 25 °C) λ_{max} nm (ε M^{-1} cm^{-1}) = 285 (21 000), 365 (12 000).

Synthesis of $(N(pi^{Cy})_3)$V (1-V)

The product was isolated as a dark green powder in good yield (82%). Crystals suitable for X-ray diffraction were grown from a concentrated ether solution of the green powder at −35 °C. HRMS (ESI) calcd for $[M + H]^+$: 630.3483 found: 630.3469. IR: 1577 cm^{-1} (C═N). μ_{eff} = 2.88(12)μ_B. UV-vis (THF, 25 °C) λ_{max} nm (ε M^{-1} cm^{-1}) = 295 (28 700), 475 (3700), 600 (2000).

Synthesis of $(N(pi^{Cy})_3)$Mo (1-Mo)

The red brown powder was isolated in moderate yield (58%). Crystals suitable for X-ray diffraction were grown from a concentrated hexanes solution of the red brown powder at −35 °C. HRMS (ESI) calcd for $[M + H]^+$: 676.3020 found: 676.3011. UV-vis (THF, 25 °C) λ_{max} nm (ε M^{-1} cm^{-1}) = 290 (55 400), 440 (1500).

Synthesis of $(N(pi^{Cy})_3)$Cr (1-Cr)

A 20 mL scintillation vial equipped with a stir bar was charged with $N(pi^{Cy})_3$ (29.2 mg, 0.05 mmol), $Cr(N(TMS)_2)_3$ (26.7 mg, 0.05 mmol), and 4 mL THF. After stirring for 2 hours, volatiles were removed under reduced pressure to give a pink residue. The product was isolated by extraction with hexanes (2 × 5 mL). Volatiles were removed under reduced pressure to give a pink powder in good yield (91%). Crystals suitable for X-ray diffraction were grown from a concentrated solution of benzene layered with hexamethyldisiloxane. HRMS (ESI) calcd for $[M + H]^+$: 631.3455 found: 631.3442. IR: ν = 1566 cm^{-1} (C═N, strong). μ_{eff} = 3.71(11)μ_B. UV-vis (THF, 25 °C) λ_{max} nm (ε M^{-1} cm^{-1}) = 290 (29 000), 365 (17 000).

Conclusions

In this study, a series of early transition metal complexes using the tripodal ligand, tris(5-cyclohexylimminopyrrol-2-ylmethyl)amine ($N(pi^{Cy})_3$), were synthesized. Our findings demonstrate the unique structural and electronic properties of these complexes, highlighting how different metal centres influence the ligand framework. The synthesis of titanium, vanadium, chromium, and molybdenum complexes (**1-Ti**, **V**, **Cr**, **Mo**) allowed us to explore and compare their distinct coordination geometries to each other and the previously published iron complex, **1-Fe**. Spectroscopic and computational analyses confirmed the metal–nitrogen bond lengths follow expected periodic trends. The absence of visible d–d transitions in the absorption spectra suggests a predominance of ligand-based transitions visible in the UV-Vis Spectra.

Overall, this work underscores the adaptability of the tripodal ligand framework, $N(pi^{Cy})_3$, and its application to the synthesis of novel metal complexes. This research contributes to the fundamental understanding of early transition metal chemistry and opens avenues for future studies exploring the reactivity of these complexes.

Author contributions

J. M. M. and T. J. M. performed experiments and characterized complexes *via* spectroscopy. J. M. M. and T. J. M. analysed spectroscopic and crystallographic data. K. L. G. aided in obtaining crystal structures. L. S. E. aided in synthesis. B. M. V. and G. N. carried out computational experiments. P. H. W. supervised computational studies. J. M. M., B. M. V., P. H. W., and A. R. F. contributed to the writing of the manuscript. A. R. F. provided funding and supervised the studies.

Conflicts of interest

There are no conflicts to declare.

Data availability

The data that support the findings in this paper are available as part of the supplementary information (SI) of this article.

Supplementary information is available. See DOI: https://doi.org/10.1039/d5dt01888a.

CCDC 2478982-2478985 contains the supplementary crystallographic data for this paper. These data can be obatined free of charge *via* www.ccdc.cam.ac.uk/structures.[47a–d]

Open Access Article. Published on 16 October 2025. Downloaded on 12/28/2025 10:30:21 AM. This article is licensed under a Creative Commons Attribution-NonCommercial 3.0 Unported Licence.

Acknowledgements

This work was supported by the U.S. Department of Energy, Office of Sciences, Office of Basic Energy Sciences, Chemical Sciences, Geosciences, and Biosciences Division under award number DOE DE-SC0025026. J. M. M. is thankful for a Hagler Fellowship from Texas A & M University. P. H. W. and B. M. V. thank Dr. Tony Wild for his support.

References

1 J. F. Riordan, *Ann. Clin. Lab. Sci.*, 1977, **7**, 119–129.
2 M. Babor, H. M. Greenblatt, M. Edelman and V. Sobolev, *Proteins: Struct., Funct., Genet.*, 2005, **59**, 221–230.
3 A. W. Foster, T. R. Young, P. T. Chivers and N. J. Robinson, *Curr. Opin. Chem. Biol.*, 2022, **66**, 102095.
4 N. Abbaspour, R. Hurrell and R. Kelishadi, *J. Res. Med. Sci.*, 2014, **19**, 164.
5 I. Schröder, E. Johnson and S. De Vries, *FEMS Microbiol. Rev.*, 2003, **27**, 427–447.
6 C. Andreini, I. Bertini, G. Cavallaro, G. L. Holliday and J. M. Thornton, *JBIC*, 2008, **13**, 1205–1218.
7 R. R. Mendel and F. Bittner, *Biochim. Biophys. Acta*, 2006, **1763**, 621–635.
8 R. Hille, *Trends Biochem. Sci.*, 2002, **27**, 360–367.
9 L. C. Seefeldt, B. M. Hoffman and D. R. Dean, *Annu. Rev. Biochem.*, 2009, **78**, 701.
10 C. S. Harwood, *Annu. Rev. Microbiol.*, 2020, **74**, 247–266.
11 G. Schwarz, R. R. Mendel and M. W. Ribbe, *Nature*, 2009, **460**, 839–847.
12 D. Niks and R. Hille, *Methods Mol. Biol.*, 2019, **1876**, 55.
13 C. Sparacino-Watkins, J. F. Stolz and P. Basu, *Chem. Soc. Rev.*, 2014, **43**, 676.
14 C. Feng, G. Tollin and J. H. Enemark, *Biochim. Biophys. Acta*, 2007, **1774**, 527.
15 D. Rehder, *Metallomics*, 2015, **7**, 730–742.
16 S. Treviño, A. Díaz, E. Sánchez-Lara, B. L. Sanchez-Gaytan, J. M. Perez-Aguilar and E. González-Vergara, *Biol. Trace Elem. Res.*, 2019, **188**, 68.
17 J. B. Vincent, *Acc. Chem. Res.*, 2000, **33**, 503–510.
18 A. S. Borovik, *Chem. Soc. Rev.*, 2011, **40**, 1870–1874.
19 J. Zhou, S. Gao and G. Hu, *Energy Fuels*, 2024, **38**, 6701–6722.
20 L. Que, *Acc. Chem. Res.*, 2007, **40**, 493–500.
21 W. Nam, *Acc. Chem. Res.*, 2007, **40**, 522–531.
22 J. Taut, J. C. Chambron and B. Kersting, *Eur. J. Inorg. Chem.*, 2023, **26**, e202200739.
23 E. M. Matson, J. A. Bertke and A. R. Fout, *Inorg. Chem.*, 2014, **53**, 4450–4458.
24 E. M. Matson, Y. J. Park and A. R. Fout, *J. Am. Chem. Soc.*, 2014, **136**, 17398–17401.
25 M. J. Drummond, T. J. Miller, C. L. Ford and A. R. Fout, *ACS Catal.*, 2020, **10**, 3175–3182.
26 C. L. Ford, Y. J. Park, E. M. Matson, Z. Gordon and A. R. Fout, *Science*, 2016, **354**, 741–743.
27 K. L. Gullett, C. L. Ford, I. J. Garvey, T. J. Miller, C. A. Leahy, L. N. Awaitey, D. M. Hofmann, T. J. Woods and A. R. Fout, *J. Am. Chem. Soc.*, 2023, **145**, 20868–20873.
28 Y. J. Park, M. N. Peñas-Defrutos, M. J. Drummond, Z. Gordon, O. R. Kelly, I. J. Garvey, K. L. Gullett, M. García-Melchor and A. R. Fout, *Inorg. Chem.*, 2022, **61**, 8182–8192.
29 J. M. Moore, T. J. Miller, M. Mu, M. N. Peñas-Defrutos, K. L. Gullett, L. S. Elford, S. Quintero, M. García-Melchor and A. R. Fout, *J. Am. Chem. Soc.*, 2025, **147**, 8444–8454.
30 H. L. Cho, K. L. Gullett and A. R. Fout, *Chem. Commun.*, 2024, **60**, 10564–10567.
31 J. M. Moore and A. R. Fout, *Chem. Sci.*, 2025, **16**, 840–845.
32 C. D'Agostino, P. Bräuer, P. Charoen-Rajapark, M. D. Crouch and L. F. Gladden, *RSC Adv.*, 2017, **7**, 36163–36167.
33 E. Ravera, L. Gigli, L. Fiorucci, C. Luchinat and G. Parigi, *Phys. Chem.*, 2022, **24**, 17397–17416.
34 R. Pigliapochi, A. J. Pell, I. D. Seymour, C. P. Grey, D. Ceresoli and M. Kaupp, *Phys. Rev. B*, 2017, **95**, 054412.
35 J. Novotny, S. Komorovsky and R. Marek, *Acc. Chem. Res.*, 2024, **57**, 1467–1477.
36 F. Neese, *Wiley Interdiscip. Rev.: Comput. Mol. Sci.*, 2012, **2**, 73–78.
37 F. Neese, T. Petrenko, D. Ganyushin and G. Olbrich, *Coord. Chem. Rev.*, 2007, **251**, 288–327.
38 S. K. Singh, J. Eng, M. Atanasov and F. Neese, *Coord. Chem. Rev.*, 2017, **344**, 2–25.
39 M. Kaupp, *J. Comput. Chem.*, 2007, **28**, 320–325.
40 R. Ketkaew, Y. Tantirungrotechai, P. Harding, G. Chastanet, P. Guionneau, M. Marchivie and D. J. Harding, *Dalton Trans.*, 2021, **50**, 1086–1096.
41 R. J. Deeth and M. Gerloch, *Inorg. Chem.*, 1985, **24**, 4490–4493.
42 E. C. Alyea, D. C. Bradley and R. G. Copperthwaite, *J. Chem. Soc., Dalton Trans.*, 1972, 1580–1584.
43 F. Weigend, *Phys. Chem. Chem. Phys.*, 2006, **8**, 1057–1065.
44 D. M. York and M. Karplus, *J. Phys. Chem. A*, 1999, **103**, 11060–11079.
45 F. Neese, F. Wennmohs, A. Hansen and U. Becker, *Chem. Phys.*, 2008, **356**, 98–109.
46 M. D. Hanwell, D. E. Curtis, D. C. Lonie, T. Vandermeersch, E. Zurek and G. R. Hutchison, *J. Cheminform.*, 2012, **4**, 17.
47 (*a*) CCDC 2478982: Experimental Crystal Structure Determination, 2025, DOI: 10.5517/ccdc.csd.cc2p6l5p; (*b*) CCDC 2478983: Experimental Crystal Structure Determination, 2025, DOI: 10.5517/ccdc.csd.cc2p6l6q; (*c*) CCDC 2478984: Experimental Crystal Structure Determination, 2025, DOI: 10.5517/ccdc.csd.cc2p6l7r; (*d*) CCDC 2478985: Experimental Crystal Structure Determination, 2025, DOI: 10.5517/ccdc.csd.cc2p6l8s.

This journal is © The Royal Society of Chemistry 2025